

monomer concentration depletes during growth, the aspect ratio gradually decreases to nearly one (ordinary quantum dots), but the short axis grows significantly. The rod morphology can be maintained (or in the case of dots, recovered) by multiple injections, which replenish the monomer, resulting in bigger quantum rods (Fig. 1c, f and g).

Transmission electron microscopy (TEM; Fig. 1) and powder X-ray diffraction (XRD; Fig. 2) confirmed the rod morphology of the resulting products. Both measurements prove that the long axis of the quantum rods is the *c*-axis of the wurtzite structure. Diffraction pattern simulations also show a much less frequent occurrence of stacking faults in the quantum rods than in spherical CdSe nanocrystals. Perpendicular to the *c*-axis, these quantum rods look like faceted hexagons under high-resolution TEM (Fig. 3). By choosing an optimal solvent/substrate combination, the *c*-axes can be aligned on a micrometre length scale, with well defined three-dimensional orientation (Fig. 3). The ability to pack and align the rods in this way will be of use in spectroscopic studies of the rods, and possibly in applications such as light-emitting diodes (LEDs) and photovoltaic cells²³.

This ability to control the shapes of semiconductor nanocrystals affords an opportunity to further test theories of quantum confinement^{24–26}, and yields samples with desirable optical characteristics from the point of view of applications. Near degeneracies in spherical dots are predicted to be lifted by elongation of the unique axis²⁷. In preliminary studies on ensembles, we have found that the splitting between absorbing and emitting states is larger in the rods than in the dots (Fig. 4a, b). This could be very helpful in applications such as LEDs where re-absorption can be a problem. Aligned nanorods in a stretched polymer at 4.7 K show polarized emission along the long axis (Fig. 4d), and this could be helpful in biological tagging experiments where the orientation of the tag needs to be determined.

The unique-axis polarized emission from the rods is in contrast to emission from round dots, for which the *c*-axis is thought to be dark²⁸. The crossover between the two regimes is of considerable theoretical interest²⁶. The quantum yield for luminescence in as-grown rods is approximately 1% at room temperature, and increases by a factor of 5 when a shell of a larger-bandgap material (CdS or ZnS) is grown on the outside of the core, as has been done with dots^{29,30}. Such quantum yields could be sufficiently high for biological labelling experiments, but are well below the maximum of 80% we have observed in dots. When thicker shells are grown, the quantum yields decrease again (Fig. 4c), possibly due to cracking or strain at the core-shell interface.

Received 6 July; accepted 17 December 1999.

1. Heath, J. M. (ed.) *Acc. Chem. Res.* **32** (Nanoscale materials special issue) (1999).
2. Alivisatos, A. P. Semiconductor clusters, nanocrystals, and quantum dots. *Science* **271**, 933–937 (1996).
3. Lieber, C. M. One-dimensional nanostructures: Chemistry, physics + applications. *Solid State Commun.* **107**, 607–616 (1998).
4. Smalley, R. E. & Yakobson, B. I. The future of the fullerenes. *Solid State Commun.* **107**, 597–606 (1998).
5. Hu, J. T., Min, O. Y., Yang, P. D. & Lieber, C. M. Controlled growth and electrical properties of heterojunctions of carbon nanotubes and silicon nanowires. *Nature* **399**, 48–51 (1999).
6. Wang, W. Z. *et al.* Synthesis and characterization of MSe (M = Zn, Cd) nanorods by a new solvothermal method. *Inorg. Chem. Commun.* **2**, 83–85 (1999).
7. Zhu, Y., Cheng, G. S. & Zhang, L. D. Preparation and formation mechanism of silicon nanorods. *J. Mater. Sci. Lett.* **17**, 1897–1898 (1998).
8. Han, W. Q., Fan, S. S., Li, Q. Q. & Hu, Y. D. Synthesis of gallium nitride nanorods through a carbon nanotube-confined reaction. *Science* **277**, 1287–1289 (1997).
9. Routkevitch, D., Bigioni, T., Moskovits, M. & Xu, J. M. Electrochemical fabrication of cds nanowire arrays in porous anodic aluminum oxide templates. *J. Phys. Chem.* **100**, 14037–14047 (1996).
10. Trentler, T. J. *et al.* Solution-liquid-solid growth of crystalline III-V semiconductors - an analogy to vapor-liquid-solid growth. *Science* **270**, 1791–1794 (1995).
11. Nishizawa, M., Menon, V. P. & Martin, C. R. Metal nanotubule membranes with electrochemically switchable ion-transport selectivity. *Science* **268**, 700–702 (1995).
12. Heath, J. R. A liquid-solution-phase synthesis of crystalline silicon. *Science* **258**, 1131–1133 (1992).
13. Ahmadi, T. S., Wang, Z. L., Green, T. C., Henglein, A. & El-Sayed, M. A. Shape-controlled synthesis of colloidal platinum nanoparticles. *Science* **272**, 1924–1926 (1996).

14. Peng, X. G., Wickham, J. & Alivisatos, A. P. Kinetics of II-VI and III-V colloidal semiconductor nanocrystal growth: "Focusing" of size distributions. *J. Am. Chem. Soc.* **120**, 5343–5344 (1998).
15. Murray, C. B., Norris, D. J. & Bawendi, M. G. Synthesis and characterization of nearly monodisperse CdE (E = S, Se, Te) semiconductor nanocrystallites. *J. Am. Chem. Soc.* **115**, 8706–8715 (1993).
16. Bruchez, M., Moronne, M., Gin, P., Weiss, S. & Alivisatos, A. P. Semiconductor nanocrystals as fluorescent biological labels. *Science* **281**, 2013–2016 (1998).
17. Chan, W. C. & Nie, S. M. Quantum dot bioconjugates for ultrasensitive nonisotopic detection. *Science* **281**, 2016–2018 (1998).
18. Schlamp, M. C., Peng, X. G. & Alivisatos, A. P. Improved efficiencies in light emitting diodes made with CdSe(CdS) core/shell type nanocrystals and a semiconducting polymer. *J. Appl. Phys.* **82**, 5837–5842 (1997).
19. Mattoussi, H. *et al.* Electroluminescence from heterostructures of poly(phenylene vinylene) and inorganic CdSe nanocrystals. *J. Appl. Phys.* **83**, 7965–7974 (1998).
20. Kolosky, M. & Vialle, J. Determination of triethylphosphine oxide and its impurities by reversed-phase high performance liquid chromatography. *J. Chromatogr.* **299**, 436–444 (1984).
21. Cortina, J. L., Miralles, N., Aguilar, M. & Sastre, A. M. Distribution studies of Zn(II), Cu(II) and Cd(II) with Lewaxrel resins containing di(2,4,4-trimethylpentyl) phosphinic acid (Lewatit TP807/84). *Hydrometallurgy* **40**, 195–206 (1996).
22. Kabay, N. *et al.* Removal of metal pollutants (Cd(II) and Cr(III)) from phosphoric acid solutions by chelating resins containing phosphonic or diphosphonic groups. *Ind. Eng. Chem. Res.* **37**, 2541–2547 (1998).
23. Huynh, W., Peng, X. & Alivisatos, A. P. CdSe nanocrystal rods/poly(3-hexylthiophene) composite photovoltaic devices. *Adv. Mater.* **11**, 923–927 (1999).
24. Zunger, A. Electronic-structure theory of semiconductor quantum dots. *Mater. Res. Bull.* **23**, 35–42 (1998).
25. Leung, K., Pokrant, S. & Whaley, K. B. Exciton fine structure in CdSe nanoclusters. *Physical Rev. B* **57**, 12291–12301 (1998).
26. Efros, A. L. *et al.* Band-edge exciton in quantum dots of semiconductors with a degenerate valence band - dark and bright exciton states. *Phys. Rev. B* **54**, 4843–4856 (1996).
27. Nirmal, M. *et al.* Observation of the dark exciton in CdSe quantum dots. *Phys. Rev. Lett.* **75**, 3728–3731 (1995).
28. Empedocles, S. A., Neuhauser, R. & Bawendi, M. G. Three-dimensional orientation measurements of symmetric single chromophores using polarization microscopy. *Nature* **399**, 126–130 (1999).
29. Peng, X. G., Schlamp, M. C., Kadavanich, A. V. & Alivisatos, A. P. Epitaxial growth of highly luminescent CdSe/CdS core/shell nanocrystals with photostability and electronic accessibility. *J. Am. Chem. Soc.* **119**, 7019–7029 (1997).
30. Dabbousi, B. O. *et al.* (CdSe)ZnS core-shell quantum dots: Synthesis and characterization of a size series of highly luminescent nanocrystallites. *J. Phys. Chem. B* **101**, 9463–9475 (1997).

Acknowledgements

This work was supported by the US Department of Energy and by the National Renewable Energy Laboratory.

Evidence from U–Th dating against Northern Hemisphere forcing of the penultimate deglaciation

Gideon M. Henderson*† & Niall C. Slowey‡

* Lamont-Doherty Earth Observatory of Columbia University, Route 9W, Palisades, New York 10964, USA

‡ Department of Oceanography, Texas A&M University, College Station, Texas 77843-3146, USA

Milankovitch proposed that summer insolation at mid-latitudes in the Northern Hemisphere directly causes the ice-age climate cycles¹. This would imply that times of ice-sheet collapse should correspond to peaks in Northern Hemisphere June insolation. But the penultimate deglaciation has proved controversial because June insolation peaks 127 kyr ago whereas several records of past climate suggest that change may have occurred up to 15 kyr earlier^{2–8}. There is a clear signature of the penultimate deglaciation in marine oxygen-isotope records. But dating this event, which is significantly before the ¹⁴C age range, has not been possible. Here we date the penultimate deglaciation in a record from the Bahamas using a new U-Th isochron technique. After the necessary

† Present address: Department of Earth Sciences, University of Oxford, South Parks Road, Oxford OX1 3PR, UK.

corrections for α -recoil mobility of ^{234}U and ^{230}Th and a small age correction for sediment mixing, the midpoint age for the penultimate deglaciation is determined to be 135 ± 2.5 kyr ago. This age is consistent with some coral-based sea-level estimates, but it is difficult to reconcile with June Northern Hemisphere insolation as the trigger for the ice-age cycles. Potential alternative driving mechanisms for the ice-age cycles that are consistent with such an early date for the penultimate deglaciation are either the variability of the tropical ocean-atmosphere system or changes in atmospheric CO_2 concentration controlled by a process in the Southern Hemisphere.

The timing of the rapid shifts in global climate and sea level that accompany the end of glacial periods is an important test of proposed driving mechanisms for the ice-age cycle. The widely

quoted SPECMAP timescale⁹ for Pleistocene ice-volume variations (as recorded by marine $\delta^{18}\text{O}$) uses a value of 127 kyr ago as the midpoint of the penultimate such deglacial event. This was based on (1) early U-Th dating of corals formed during the sea-level highstand following the deglaciation, and (2) the assumption, after Milankovitch¹, that variations of Northern Hemisphere insolation at 60°N caused the changes in sea level. Recent work has suggested this age may be too late. Further dating of coral terraces has placed the peak of sea level at 128–122 kyr (ref. 2), and several studies have suggested that sea level was above the modern value as early as 135 kyr (refs 2–8). Ice-flow age models for the Vostok ice core also typically place the penultimate deglaciation at >127 kyr, although there is uncertainty about which model is most valid^{10–13}. And a record of terrestrial climate preserved in a cave deposit at Devils

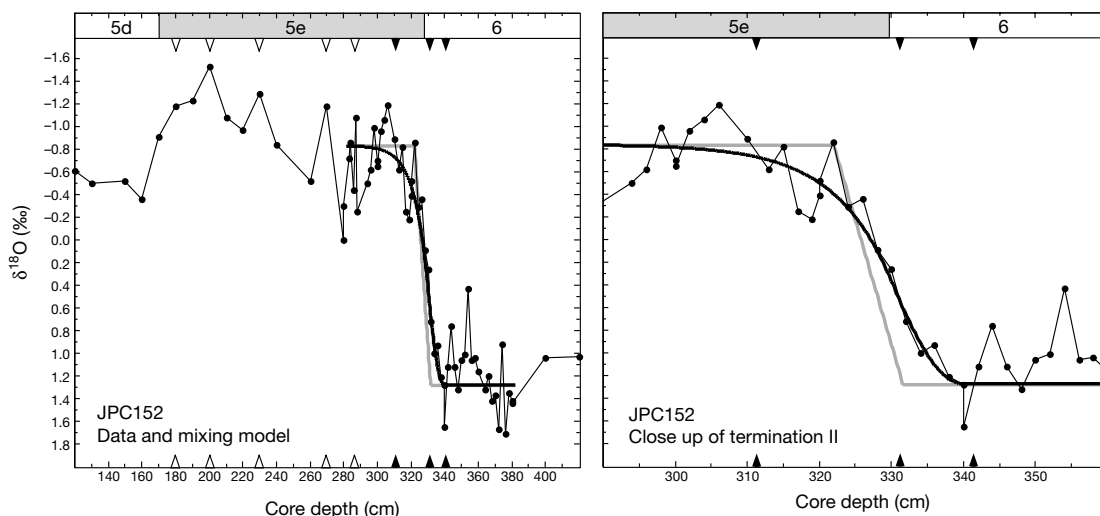


Figure 1 Oxygen-isotope stratigraphy for Bahamas core JPC152 on two different depth scales. Data points are the average of at least two replicate measurements, each on three or four *Globigerinoides sacculifer*. Shaded bars above the figures show the marine (oxygen) isotope stages (MIS). Black arrowheads mark the depths of samples dated in this study, and white arrowheads are bulk sample ages from Slowey *et al.*¹⁶. Sediment mixing increases the apparent duration and midpoint age of the deglaciation. These effects are pronounced for Bahamas slope sediments because of the rapid increase in sedimentation rate between glacial and interglacial times. The mixed layer on the slopes of the Little Bahama Bank is 8 cm thick³⁰. Solid lines in the figure are the unmixed (grey) and mixed (black) $\delta^{18}\text{O}$ curves from a simple forward model assuming efficient mixing through an 8-cm layer. Mixing is applied to both the $\delta^{18}\text{O}$ and to the age of the sediment. The mixing

model assumes a sedimentation rate of 1.5 cm kyr^{-1} in MIS 6 and 12 cm kyr^{-1} in MIS 5e (derived from the thickness of MIS 6 and MIS 5e in JPC152¹⁶). The switch in sedimentation rate is assumed to occur when full MIS 5e conditions are reached as this is approximately the timing of bank flooding. Secondary details of the deglaciation cannot be reconstructed with only three dated horizons so we assume a simple linear change in $\delta^{18}\text{O}$ from MIS 6 to MIS 5e. The duration of this change is adjusted to give a good fit to the data. Durations of between 4 and 7 kyr provide a reasonable fit to the $\delta^{18}\text{O}$ data, and also fit well with the isochron ages in this study (Fig. 3a). Adjusting parameters such as sedimentation rates in the model may alter the deglacial duration somewhat, but any reasonable input results in a midpoint of the deglaciation of 135.2 ± 2.5 kyr.

Table 1 U-Th results and 2σ errors from Bahamas core JPC152

Core-depth	^{238}U (p.p.m.)	$(^{234}\text{U}/^{238}\text{U})$	^{232}Th (p.p.b.)	$(^{230}\text{Th}/^{232}\text{Th})$ measured	f^{234}	$(^{230}\text{Th}/^{232}\text{Th})$ corrected
<i>JPC152-311cm</i>						
2.70–2.75 g cm ⁻³	2.7746 ± 0.0023	1.1628 ± 0.0033	210.8 ± 0.7	42.01 ± 0.22	1.195 ± 0.011	34.45 ± 0.42
2.75–2.80 g cm ⁻³	4.5767 ± 0.0037	1.1037 ± 0.0028	148.7 ± 0.3	80.65 ± 0.33	1.006 ± 0.007	80.07 ± 0.73
>2.80 g cm ⁻³	3.8656 ± 0.0041	1.0975 ± 0.0030	102.4 ± 0.4	91.03 ± 0.39	0.986 ± 0.008	92.45 ± 0.89
bulk sediment	4.7984 ± 0.0036	1.1012 ± 0.0027				
<i>JPC152-331cm</i>						
2.70–2.75 g cm ⁻³	0.7203 ± 0.0004	1.1345 ± 0.0034	222.9 ± 1.2	10.03 ± 0.10	1.106 ± 0.010	8.96 ± 0.13
2.75–2.80 g cm ⁻³	1.1456 ± 0.0010	1.1203 ± 0.0032	291.1 ± 2.7	11.98 ± 0.16	1.062 ± 0.009	11.20 ± 0.19
>2.80 g cm ⁻³	2.6079 ± 0.0019	1.0855 ± 0.0030	62.8 ± 0.1	97.39 ± 0.51	0.953 ± 0.007	102.79 ± 0.96
Pteropods	0.5645 ± 0.0003	1.1353 ± 0.0027	242.6 ± 1.1	7.84 ± 0.09	1.108 ± 0.008	6.99 ± 0.11
Bulk sediment	2.2356 ± 0.0014	1.1134 ± 0.0027				
<i>JPC152-341cm</i>						
2.70–2.75 g cm ⁻³	0.5037 ± 0.0002	1.1221 ± 0.0032	237.8 ± 0.9	7.45 ± 0.07	1.071 ± 0.009	6.89 ± 0.09
2.75–2.80 g cm ⁻³	1.0329 ± 0.0007	1.1178 ± 0.0034	299.7 ± 2.0	11.46 ± 0.20	1.058 ± 0.009	10.76 ± 0.22
>2.80 g cm ⁻³	2.5105 ± 0.0014	1.0900 ± 0.0035	69.1 ± 0.1	90.11 ± 0.32	0.975 ± 0.008	92.70 ± 0.88
Pteropods	0.5112 ± 0.0002	1.1247 ± 0.0029	239.3 ± 1.0	7.40 ± 0.10	1.079 ± 0.008	6.80 ± 0.12
Bulk sediment	1.1827 ± 0.0006	1.0995 ± 0.0037				

Core location: latitude 26.2267° N, longitude 77.6708° W, 577 m. f^{234} is the fraction of radiogenic ^{234}U which remains in the subsample (that is, values <1 mean that some ^{234}U is lost by recoil, while values >1 mean addition). Corrected $(^{230}\text{Th}/^{232}\text{Th})$ values are adjusted for recoil effects on ^{230}Th using f^{234} (see Methods).

Hole, Nevada, places the midpoint of the deglaciation at 142 kyr (refs 14, 15). Devils Hole is the best dated of these records, but linking the stable-isotope signal preserved there to global climate is problematic. If global climate did change significantly before 127 kyr, the penultimate deglaciation could not have been caused simply by high June Northern Hemisphere insolation, and a more complex linkage between insolation and climate must be invoked. The penultimate deglaciation is well preserved in marine $\delta^{18}\text{O}$ records but dating these records beyond the ^{14}C age range has not been possible, preventing an assessment of the timing of this important event.

Aragonite-rich sediments from the slopes of the Bahamas have recently yielded precise U–Th ages for the last interglacial¹⁶. With the bulk sediment technique used to obtain those ages, however, it was not possible to date the deglaciation preceding this interglacial. The main analytical problem to overcome in order to extend dating to this deglaciation is the separation of three sources of ^{230}Th . Radiogenic ^{230}Th , of interest for dating, must be distinguished from detrital ^{230}Th and from ^{230}Th scavenged from sea water. These last two contaminating sources of ^{230}Th also contribute ^{232}Th to the sediment, suggesting the possibility of U–Th isochron dating but, unfortunately, the two sources of contamination do not have the same $^{232}\text{Th}/^{230}\text{Th}$ ratio. Before an isochron technique can be applied, therefore, one of the sources of contamination must be accurately corrected for, or completely removed. An earlier attempt to correct isochrons for detrital ^{230}Th using aluminium measurements resulted in large corrections and uncertainty on the final age that was unacceptably high¹⁷. Here we instead quantitatively remove detrital material before analysis by a careful washing protocol. The resulting washed samples contain a mixture of radiogenic and scavenged Th which can be distinguished using an isochron.

To create the range of U/Th ratios required to construct isochrons from the washed samples, heavy-liquid separation was used to concentrate aragonite, high-Mg calcite, and low-Mg calcite into three subsamples. To assess whether these subsamples are the same age as one another, a prerequisite for isochron dating, separation was performed on a sample from the last glacial. AMS (accelerator

mass spectrometry) ^{14}C dates for the three fractions were $25,300 \pm 90$ years, $25,200 \pm 190$ years and $24,100 \pm 160$ years. The reasonable agreement between these ages indicates that using such separates for isochron dating is valid. The similarity of the ages to one another also argues against the presence of allochthonous grains in the sediment. Such allochthonous material was minimized by selecting a core from an area where no downslope transport is observed to have occurred in the latest Quaternary¹⁸. The agreement in $\delta^{18}\text{O}$ stratigraphy measured on foraminifera and fine-fraction sediment at this location provides further evidence that all sediment is directly deposited¹⁶. In order to test the isochron approach, two samples from within the ^{14}C age range were dated with the full approach outlined below. One sample was from the Holocene and the other from close to the midpoint of the most recent deglaciation. Isochron ages for these two samples are 3.3 ± 0.8 kyr and 13.0 ± 0.6 kyr ago. These dates agree with the ^{14}C chronology of the core from which samples were taken, and the age for the deglacial sample fits well with the timing of this event¹⁹. This gives us confidence that the isochron technique provides reliable ages.

To date the penultimate deglaciation, the resolution of the $\delta^{18}\text{O}$ stratigraphy for this interval was first improved (Fig. 1). Samples were then selected from the end of marine oxygen isotope stage (MIS) 6, half way through the deglaciation, and the beginning of MIS 5e (Methods; Table 1). For each of these three isochrons, subsample ($^{234}\text{U}/^{238}\text{U}$), where parentheses indicate activity ratio, varies systematically with U/Th ratio (Fig. 2). This variation cannot be explained by the presence of detrital material, even if some has escaped the pretreatment, as subsamples with low U/Th have high ($^{234}\text{U}/^{238}\text{U}$). When compared to the ($^{234}\text{U}/^{238}\text{U}$) expected at ~ 130 kyr, subsamples with high U/Th are impoverished in ^{234}U while low-U/Th samples are enriched. Addition or removal of U from the sediment cannot readily explain this systematic variation. As a test for such addition or removal of U, however, bulk sediment ($^{234}\text{U}/^{238}\text{U}$) was also analysed for each sample. Two of the samples have ($^{234}\text{U}/^{238}\text{U}$) within error of that expected, and the third is reasonably close. Older samples from the same core also show bulk sediment ($^{234}\text{U}/^{238}\text{U}$) close to that expected¹⁶. These bulk sediment

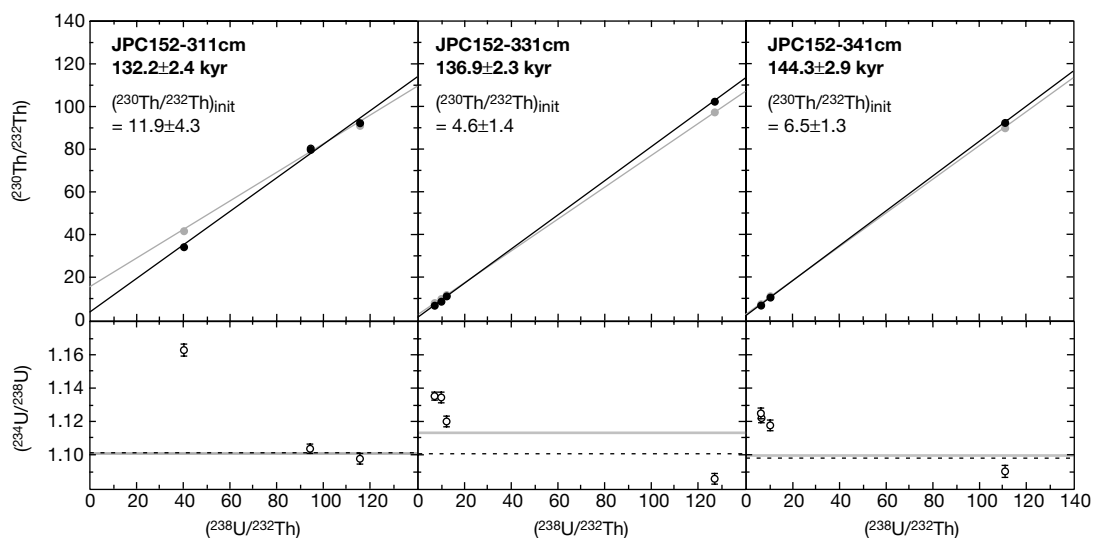


Figure 2 Isochrons and U-isotope ratios from the penultimate deglaciation. Upper panels, U–Th isochrons for three horizons in Bahamas core JPC152 (Fig. 1). Grey points and lines are measured data, black points and lines are data after correction for the effects of α -recoil (see Methods). $^{238}\text{U}/^{232}\text{Th}$ isochrons rather than $^{234}\text{U}/^{238}\text{U}$ isochrons are plotted because of the mobility of ^{234}U in these sediments. The initial thorium-isotope ratio, $(^{230}\text{Th}/^{232}\text{Th})_{\text{init}}$, calculated from the MIS 5e (311 cm) isochron, is within error of the seawater value for the Holocene¹⁶, increasing confidence that non-radiogenic Th is

derived solely from sea water. Lower panels, subsample ($^{234}\text{U}/^{238}\text{U}$) versus U/Th illustrating the effects of α -recoil. The dashed line represents the expected ($^{234}\text{U}/^{238}\text{U}$) for sediment of the age given by the isochron above. Grey lines represent the measured ($^{234}\text{U}/^{238}\text{U}$) for bulk sediment. The reasonable agreement between expected and measured ($^{234}\text{U}/^{238}\text{U}$) supports the idea that subsample deviations in ($^{234}\text{U}/^{238}\text{U}$) are due to α -recoil redistribution of ^{234}U .

data indicate that, although individual grains show altered ($^{234}\text{U}/^{238}\text{U}$), sediment at a centimetre scale has remained a closed system.

The systematic variation of ($^{234}\text{U}/^{238}\text{U}$) is well explained by internal reorganization of ^{234}U due to α -recoil. Subsamples with high U/Th values preferentially lose ^{234}U while low-U/Th subsamples gain ^{234}U . As the energy of decay of ^{234}U and ^{238}U are rather similar, ^{230}Th will be redistributed in a manner similar to ^{234}U . We are fortunate that both ^{234}U and ^{230}Th form from the decay of U which is initially incorporated with a uniform ($^{234}\text{U}/^{238}\text{U}$) ratio. This means that, regardless of the distribution of U within the grains, the recoil mobility of ^{234}U (from ^{238}U decay) tells us directly about the recoil mobility of ^{230}Th (from ^{234}U decay). The process of recoil exchange is dependent only on the rate of decay of the two U nuclides. It should also be noted that the initial decay product is an isotope of thorium in both cases (^{234}Th and ^{230}Th). So any exchange that occurs via pore waters rather than by direct grain-to-grain exchange will be chemically identical for both daughters and fast (due to the very strong tendency for thorium to adhere to particles). Deviations of the ($^{234}\text{U}/^{238}\text{U}$) ratio from that expected can therefore be used to make an entirely self-consistent correction to the ^{230}Th concentrations in the subsamples (see Methods). This correction has the effect of steepening the $^{230}\text{Th}/^{238}\text{U}$ isochrons by 15%, 7% and 4% respectively for the three isochrons (Fig. 2). The difference in the magnitude of the effect between the three isochrons is well explained by the grain size of the sediment, which is significantly finer in highstand sediment. Overall, the size of the recoil effect is larger than would be expected if U were distributed uniformly within grains of this size (63–250 μm). This observation is consistent with evidence that much of the U in these Bahamas sediments is contained in an organic phase which coats the grains²⁰.

Isochron ages corrected for the effects of α -recoil are 132.2 ± 2.4 kyr, 136.9 ± 2.3 kyr and 144.3 ± 2.9 kyr ago. Uncertainties are 2σ and are fully discussed in the Methods section. Several arguments support the validity of these ages. The internal consistency of the data argues against diagenesis, which would raise the bulk ($^{234}\text{U}/^{238}\text{U}$) value and destroy the linearity of the isochrons. The youngest isochron yields an age which fits well with the bulk-sediment U–Th age from directly above it in the same core¹⁶. This isochron requires the largest correction for recoil, so its realistic age argues strongly for the validity of the correction. Unlike corals, these samples have never been exposed to air or been in contact with meteoric water. The sediment environment can be directly investigated by measurement of U isotopes and concentrations in the pore waters of Bahamas sediment²⁰. Such analyses show that U concentrations in pore waters are more than 1,000 times lower than in the sediments analysed here. Mass balance calculations based on these porewater data indicate that, even allowing for the periodic fluid-flow which has occurred through these sediments, insignificantly small amounts of U are mobile within this sedimentary environment.

Before the isochron ages can be used to assess the timing of the penultimate deglaciation, a small correction must be made for bioturbation. Mixing increases the apparent duration and midpoint age of the deglaciation, the latter by slightly more than 1 kyr (Fig. 1). After unmixing, and allowing for uncertainty in the isochron ages, the midpoint of the penultimate deglaciation is 135.2 ± 2.5 kyr. This age is some 8 kyr older than the SPECMAP value, but is consistent with some coral data (Fig. 3). Using corals to date the end of the penultimate deglaciation directly is difficult. Relative local sea level must be corrected for the regionally variable effect of isostatic unloading²¹. Coral diagenesis and possible inaccuracy in uplift history add further complications, and mean that individual coral datum points are open to question. Corals from within ~ 30 m of peak MIS 5e sea level have, however, provided U–Th ages greater than 130 kyr in several regions^{2–8} (Fig. 3). While uncertain of the diagenetic integrity of such coral samples, Stirling *et al.*²² used an

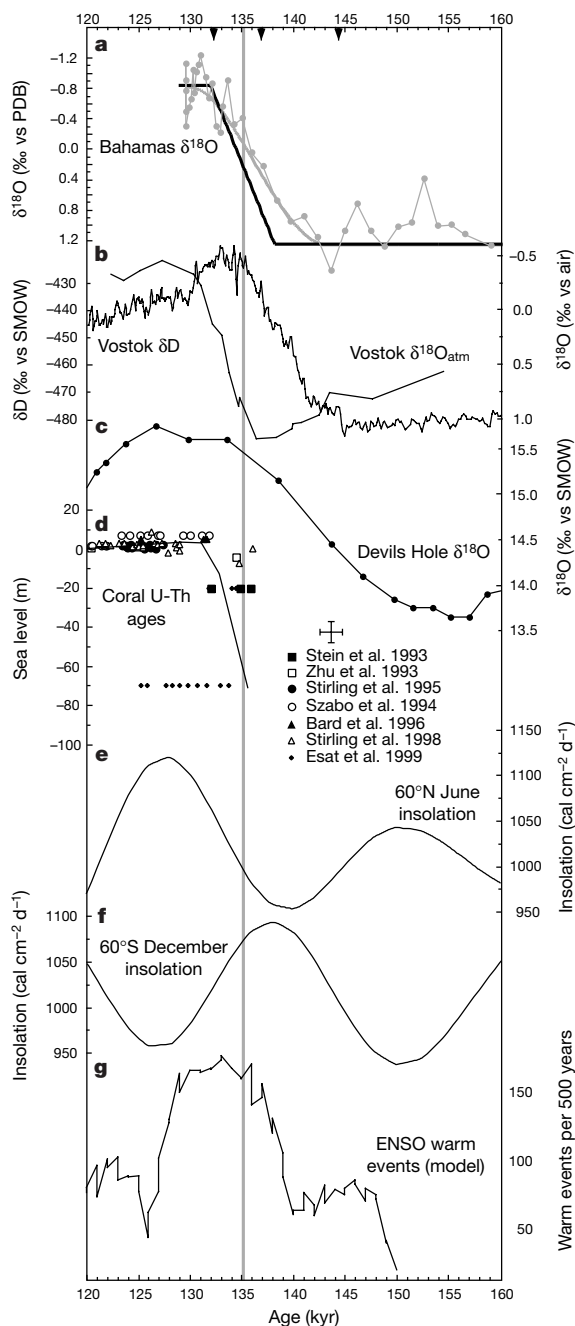


Figure 3 Timing comparison of the marine $\delta^{18}\text{O}$ record of deglaciation with data from elsewhere. **a**, $\delta^{18}\text{O}$ against age derived from U–Th isochrons at the three horizons marked by black arrowheads on the top, horizontal axis. The solid grey line is a model fit to the $\delta^{18}\text{O}$ data, and the black line is the unmixed version of this model. The midpoint of the deglaciation occurs at 135.2 ± 2.5 kyr, and is marked by the vertical grey bar. **b**, Vostok δD (ref. 11) plotted on the original Lorius timescale¹⁰ together with Vostok $\delta^{18}\text{O}_{\text{atm}}$ of atmospheric O_2 , $\delta^{18}\text{O}_{\text{atm}}$ (ref. 12), plotted on a gas-age timescale consistent with the Lorius timescale²⁴. **c**, The Devils Hole $\delta^{18}\text{O}$ record¹⁵. **d**, A compilation of select coral U–Th ages versus reconstructed sea level from listed references. Only data with ($^{234}\text{U}/^{238}\text{U}$) less than or equal to 1.160 are included. The cross above the key is representative of the error on such data. No sea-level estimate was given by Bard *et al.* but these samples were from the last interglacial terrace and have therefore been placed at +5 m. Black lines represent a sea-level curve for sites far from ice-loading effects based on such coral data²². The data at -70 m have been suggested to represent a dramatic reversal in sea level after the initial rise⁷. The large spread in ages for samples from a single locality may also suggest the presence of diagenesis. **e**, **f**, Insolation curves for summer months at 60°N and 60°S . **g**, Number of warm ENSO events per 500 years in an orbitally forced model of the tropical Pacific²⁷.

isostatic model to show that, taken at face value, they required a midpoint age for the penultimate rise in sea level of ~135 kyr. The broad timing agreement between this coral-based sea-level record and that derived here from marine $\delta^{18}\text{O}$ provides further support for the validity of the isochron ages derived in this study.

The deglacial age of 135 kyr can be used to test the various age models for the Vostok ice core^{10–13}. Atmospheric $\delta^{18}\text{O}$ values ($\delta^{18}\text{O}_{\text{atm}}$), as recorded in air bubbles in Vostok¹², are a possible proxy for marine $\delta^{18}\text{O}$, but lag by ~2 kyr due to the atmospheric residence time of O_2 (refs 12, 23). Early Vostok chronologies^{10,24} place the midpoint of the penultimate deglacial shift at ~133 kyr, 2 kyr later than the midpoint of the marine $\delta^{18}\text{O}$ as derived here and therefore in good agreement. This suggests that the early Lorius timescale¹⁰ for Vostok is broadly correct, and places the midpoint of warming at Vostok (as recorded by δD) at 138–139 kyr. The 142-kyr midpoint of the well-dated Devils Hole record^{14,15} is clearly older than the midpoint of the marine $\delta^{18}\text{O}$ change.

Deglaciation centred at 135.2 ± 2.5 kyr is difficult to reconcile with an ice-age cycle triggered directly by Northern Hemisphere June insolation. A more indirect role for changes in insolation must be sought. Whereas June insolation at 60°N is below average at 135 kyr and does not peak until 127 kyr, summer insolation in the Southern Hemisphere peaks at 138 kyr (Fig. 3). The change in global atmospheric CO_2 concentration closely follows δD , and is centred at 138–139 kyr, coincident with the peak in Southern Hemisphere insolation (Fig. 3). This relationship suggests that the change in CO_2 is driven by a process in the Southern Hemisphere²³. This change in CO_2 may initiate the processes that eventually lead to the collapse of the Northern Hemisphere ice sheets. Southern Hemisphere mechanisms for the ice-age cycle are also suggested by the pattern of phasing between Southern Ocean sea surface temperature changes and $\delta^{18}\text{O}$ (ref. 25), and are consistent with possible effects of sea-ice variability²⁶. An alternative to Southern Hemisphere control of ice-sheet collapse which is also consistent with the timescale derived here, is involvement of the tropical ocean–atmosphere system. Recent modelling suggests that increasing insolation leads to a larger than average number of El Niño/Southern Oscillation (ENSO) warm events, starting at ~137 kyr ago (Fig. 3)²⁷.

Methods

Detrital material was removed from ~10-g samples of Bahamas sediment by sieving and repeatedly washing at 63–250 μm . Subsamples were then separated by centrifuging in sodium polytungstate solution at the densities shown in Table 1. Pteropod samples were hand-picked from the >250- μm fraction and thoroughly cleaned. U and Th isotopes were analysed using a VG Sector-54 thermal ionization mass spectrometer. Concentrations were measured by addition of a mixed ^{229}Th – ^{230}U spike calibrated versus the secular equilibrium standard $\text{HU}-1^{14}$. U-500 standards interspersed between these analyses gave $^{235}\text{U}/^{238}\text{U} = 95.76 \pm 0.37$ (2 s.d.; $n = 14$). Blanks for the entire procedure, including heavy liquid separation, are 139 pg ^{232}Th and 760 pg ^{238}U , with $^{234}\text{U}/^{238}\text{U} \approx 1$. Decay constants used are $\lambda^{234} = 2.835 \times 10^{-6}$, $\lambda^{238} = 1.551 \times 10^{-10}$ and $\lambda^{230} = 9.195 \times 10^{-6}$.

Isochrons were corrected for the effects of α -recoil as follows. There are three unknowns: initial ($^{234}\text{U}/^{238}\text{U}$), age, and the fraction of daughter product (f) that remains in the sample after recoil. We assume that all grains started with ($^{234}\text{U}/^{238}\text{U}$) equal to the modern seawater value of 1.148. The seawater value is not thought to have changed significantly over the last 200 kyr (refs 8, 28) but the effects of small changes are investigated below. This leaves two unknowns and two measured quantities ($^{230}\text{Th}/^{238}\text{U}$ and $^{234}\text{U}/^{238}\text{U}$), so we can solve for age and f .

From the equation for decay in a radioactive series assuming that $\lambda^{238} \ll \lambda^{234}$, it can be shown that:

$$f^{234} = \frac{(^{234}\text{U}/^{238}\text{U}) - 1.148 e^{-\lambda^{234}t}}{1 - e^{-\lambda^{234}t}} \quad (1)$$

where t is the age of the sample. As the average energy of ^{238}U decay (4.184 eV; ref. 29) is not identical to ^{234}U decay (4.754 eV), we correct using:

$$\frac{1 - f^{234}}{1 - f^{230}} = \frac{\alpha^{234} M^{230}\text{Th}}{\alpha^{230} M^{234}\text{Th}} \quad (2)$$

where α is alpha decay energy released on formation of the two nuclides, and M is the mass of the recoiled nuclides. We use f^{230} calculated for each subsample in the following equation, derived from the equation of decay in a radioactive series:

$$\left(\frac{^{230}\text{Th}}{^{238}\text{U}}\right) = f^{230} \left(1 - e^{-\lambda^{230}t}\right) + \frac{f^{230} \lambda^{230}}{\lambda^{230} - f^{230} \lambda^{234}} \times 0.148 \left(e^{-f^{230} \lambda^{234}t} - e^{-\lambda^{230}t}\right) \quad (3)$$

We solve these three equations iteratively: f^{230} is initially set to 1, t is calculated for each sample using an isochron and $(^{234}\text{U}/^{238}\text{U})_{\text{init}} = 1.148$; deviations of $(^{234}\text{U}/^{238}\text{U})$ from that expected for a sample of age t are used to calculate f^{234} for each subsample (equation (1)); f^{230} is recalculated for each subsample (equation (2)); $(^{230}\text{Th}/^{238}\text{U})$ values are recalculated using this new f^{230} (equation (3)); t is recalculated with an isochron; and the process repeated until t and f are stationary (Table 1; Fig. 2).

Quoted errors are 2σ random error on the isochron ages, and are calculated as the quadratic sum of uncertainty due to the slope of the isochron and the recoil correction. The latter is assessed from the uncertainty in the measured ($^{234}\text{U}/^{238}\text{U}$), and is the largest contributor to the final error. Additional systematic error may be introduced if detrital material survives the pretreatment, or if past seawater had a different ($^{234}\text{U}/^{238}\text{U}$) value. If detrital material is found in all subsamples of an isochron in equal amounts, it will not bias the age. But if it occurs only in the less-dense fractions, it will cause a positive initial age. The magnitude of this effect was investigated for the 144.2-kyr isochron by assuming that 5% of the initial ^{232}Th was detrital for the three low-U/Th subsamples. This makes only a 0.25-kyr change to the age, and is therefore not significant. The survival of more than 5% detrital Th through the pretreatment is unlikely, as (1) the subsamples dissolved in weak acid and as (2) isochrons yield $(^{232}\text{Th}/^{230}\text{Th})_{\text{init}}$ values which agree with modern sea water. The effect of a 2% higher seawater ($^{234}\text{U}/^{238}\text{U}$) value at the last interglacial has also been assessed. This leads to ages for the three isochrons that are only ~0.35 kyr younger.

Received 29 April; accepted 30 December 1999.

- Milankovitch, M. in *Handbuch der Klimatologie* (eds Koppen, W. & Geiger, R.) 1–176 (Gebruder Borntraeger, Berlin, 1930).
- Stirling, C. H., Esat, T. M., Lambeck, K. & McCulloch, M. T. Timing and duration of the Last Interglacial: Evidence for a restricted interval of widespread coral reef growth. *Earth Planet. Sci. Lett.* **160**, 745–762 (1998).
- Stein, M. et al. TIMS U-series dating and stable isotopes of the last interglacial event in Papua New Guinea. *Geochim. Cosmochim. Acta* **57**, 2541–2554 (1993).
- Zhu, Z. R. et al. High-precision U-series dating of last interglacial events by mass spectrometry: Houtman Abrolhol Islands, western Australia. *Earth Planet. Sci. Lett.* **118**, 281–293 (1993).
- Szabo, B. J., Ludwig, K. R., Muhs, D. R. & Simmons, K. R. Thorium-230 ages of corals and duration of the last interglacial sea-level high stand on Oahu, Hawaii. *Science* **266**, 93–96 (1994).
- Bard, E. et al. Pleistocene sea levels and tectonic uplift based on dating of corals from Sumba Island, Indonesia. *Geophys. Res. Lett.* **23**, 1473–1476 (1996).
- Esat, T. M., McCulloch, M. T., Chappell, J., Pillans, B. & Omura, A. Rapid fluctuations in sea level recorded at Huon Peninsula during the penultimate deglaciation. *Science* **283**, 197–201 (1999).
- Gallup, C. D., Edwards, R. L. & Johnson, R. G. The timing of high sea levels over the past 200,000 years. *Science* **263**, 796–800 (1994).
- Imbrie, J. et al. in *Milankovitch and Climate* (eds Berger, A., Imbrie, J., Hays, J., Kukla, G. & Saltzman, B.) 269–305 (Reidel, Dordrecht, 1984).
- Lorius, C. et al. A 150,000-year climatic record from Antarctic ice. *Nature* **316**, 591–596 (1985).
- Jouzel, J. et al. Extending the Vostok ice-core record of palaeoclimate to the penultimate glacial period. *Nature* **364**, 407–412 (1993).
- Sowers, T. et al. A 135,000-year Vostok-Specmap common temporal framework. *Paleoceanography* **8**, 737–766 (1993).
- Petit, J. R. et al. Climate and atmospheric history of the past 420,000 years from the Vostok ice core, Antarctica. *Nature* **399**, 429–436 (1999).
- Ludwig, K. R. et al. Mass-spectrometric ^{230}Th – ^{234}U dating of the Devils Hole calcite vein. *Science* **258**, 284–287 (1992).
- Winograd, I. J., Landwehr, J. M., Ludwig, K. R., Coplen, T. B. & Riggs, A. C. Duration and structure of the past four interglaciations. *Quat. Res.* **48**, 141–154 (1997).
- Slowey, N. C., Henderson, G. M. & Curry, W. B. Direct U–Th dating of marine sediments from the two most recent interglacial periods. *Nature* **383**, 242–244 (1996).
- Henderson, G. M. & Slowey, N. C. U–Th isochron dating of the marine oxygen-isotope record. *Mineral. Mag.* **62**, 602–603 (1998).
- Burns, S. & Neumann, A. C. Pelagic sedimentation on an inactive gullied slope, Northwest Providence Channel, Bahamas. *Mar. Geol.* **77**, 277–286 (1987).
- Bard, E., Hamelin, B., Fairbanks, R. G. & Zindler, A. Calibration of the ^{14}C timescale over the past 30,000 years using mass spectrometric U–Th ages from Barbados corals. *Nature* **345**, 405–410 (1990).
- Henderson, G. M., Slowey, N. C. & Haddad, G. A. Fluid flow through carbonate platforms: Constraints from $^{234}\text{U}/^{238}\text{U}$ and Cl^- in Bahamas pore-waters. *Earth Planet. Sci. Lett.* **169**, 99–111 (1999).
- Lambeck, K. & Nakada, M. Constraints on the age and duration of the last interglacial period and on sea-level variations. *Nature* **357**, 125–128 (1992).
- Stirling, C. H., Esat, T. M., McCulloch, M. T. & Lambeck, K. High-precision U-series dating of corals from Western Australia and implications for the timing and duration of the last Interglacial. *Earth Planet. Sci. Lett.* **135**, 115–130 (1995).
- Broecker, W. S. & Henderson, G. M. The sequence of events surrounding Termination II and their implications for the cause of glacial-interglacial CO_2 change. *Paleoceanography* **13**, 352–364 (1998).
- Barnola, J. M., Pimienta, P., Raynaud, D. & Korotkevich, Y. S. CO_2 -climate relationship as deduced from the Vostok ice core: A re-examination based on new measurements and on a re-evaluation of the air dating. *Tellus B* **43**, 83–90 (1991).
- Hays, J. D., Imbrie, J. & Shackleton, N. J. Variations in the Earth's orbit: Pacemaker of the ice ages. *Science* **194**, 1121–1132 (1976).
- Kim, S. J., Crowley, T. J. & Stossel, A. Local orbital forcing of Antarctic climate change during the Last Interglacial. *Science* **280**, 728–730 (1998).
- Clement, A., Seager, R. & Cane, M. Orbital controls on ENSO and the tropical climate. *Paleoceanography* **14**, 441–456 (1999).
- Henderson, G. M., Cohen, A. S. & O'Nions, R. K. $^{234}\text{U}/^{238}\text{U}$ ratios and ^{230}Th ages for Hateruma Atoll

- corals: implications for coral diagenesis and seawater $^{234}\text{U}/^{238}\text{U}$ ratios. *Earth Planet. Sci. Lett.* 115, 65–73 (1993).
29. Ivanovich, M. & Harmon, R. S. *Uranium-series Disequilibrium: Applications to Earth, Marine, and Environmental Sciences* (Oxford Univ. Press, 1992).
30. Henderson, G. M., Lindsay, F. & Slowey, N. C. Variation in bioturbation with water depth on marine slopes: A study on the slopes of the Little Bahamas Bank. *Mar. Geol.* 160, 105–118 (1999).

Acknowledgements

We thank D. Schrag, R. Anderson, N. Shackleton and T. Crowley for discussion and comments, and M. Yeager for technical assistance. This work was supported by the US National Science Foundation.

Correspondence and requests for materials should be addressed to G.M.H. (e-mail: gideonh@earth.ox.ac.uk).

Stable sulphate clusters as a source of new atmospheric particles

Markku Kulmala, Liisa Pirjola & Jyrki M. Mäkelä

University of Helsinki, Department of Physics, PO Box 9, FIN-00014, University of Helsinki, Finland

The formation of new atmospheric particles with diameters of 3–10 nm has been observed at a variety of altitudes and locations. Such aerosol particles have the potential to grow into cloud condensation nuclei, thus affecting cloud formation as well as the global radiation budget. In some cases, the observed formation rates of new particles have been adequately explained by binary nucleation, involving water and sulphuric acid¹, but in certain locations—particularly those within the marine boundary layer^{1,2} and at continental sites^{1,3}—observed ambient nucleation rates exceed those predicted by the binary scheme. In these locations, ambient sulphuric acid (H_2SO_4) levels are typically lower than required for binary nucleation¹, but are sufficient for ternary nucleation⁴ (sulphuric acid–ammonia–water). Here we present results from an aerosol dynamics model with a ternary nucleation scheme which indicate that nucleation in the troposphere should be ubiquitous, and yield a reservoir of thermodynamically stable clusters 1–3 nm in size. We suggest that the growth of these clusters to a detectable size (> 3 nm particle diameter) is restricted by the availability of condensable vapour. Observations of atmospheric particle formation and growth from a continental and a coastal site support this hypothesis, indicating that a growth process including ternary nucleation is likely to be responsible for the formation of cloud condensation nuclei.

The importance of atmospheric aerosols to the global radiation balance, to cloud formation, and to alleged human health effects has motivated several recent studies on aerosol formation. Bursts of recently formed particles have been observed in several regions around the world, for example, in the free troposphere^{1,5–7}, in the marine boundary layer^{2,8–11}, at coastal sites¹², in the vicinity of evaporating clouds^{11,13}, in Arctic areas^{14,15}, in urban areas and in stack plumes^{16,17}, and in boreal forests^{3,18}. Several nucleation mechanisms have been proposed to explain this particle production, along with meteorological-related nucleation-enhancement processes such as turbulent fluctuations, waves and mixing^{19,20}.

Typically, the formation of atmospheric aerosols is attributed to binary nucleation of water and sulphuric acid^{21–23}. However, the binary theory is able to predict the nucleation rates only at some extreme conditions of low temperatures, high relative humidities, small pre-existing aerosol concentrations and at high sulphuric acid concentrations. The recently developed ternary nucleation model^{4,24} of sulphuric acid–ammonia–water (H_2SO_4 – NH_3 – H_2O)

gives significantly higher nucleation rates and thus predicts nucleation under typical tropospheric sulphuric acid (10^5 – 10^7 cm⁻³; refs 1 and 10) and ammonia (a few p.p.t.) concentrations. Although they use different thermodynamical data (vapour pressures, surface tension) both models^{4,24} are in reasonable agreement—showing, for example, the importance of sulphuric acid molecules in the nucleation process and the effect of ammonia. Model calculations indicate that ternary nucleation happens very easily in the daytime, thus raising the question: why do we not observe new particle production as often in the atmosphere?

The answer to this is that, as a result of measurement instrumentation limitations, newly formed particles of ~ 1 nm have first to grow to detectable sizes of ~ 3 nm. Whereas ternary nucleation achieves similar particle nucleation rates to the binary scheme, with approximately 1,000 times less sulphuric acid (see Fig. 1), the corresponding condensational growth of nucleated particles will take 1,000 times longer. At such a low gas-phase concentration of H_2SO_4 , it will take several days to grow the nucleated particles up to detectable sizes. Consequently, additional vapours, other than sulphuric acid and ammonia, are required to account for particle growth.

Here we present the following hypothesis, which—in principle—enables us to explain all observed particle production bursts in the atmosphere: (1) In the atmosphere, nucleation is occurring almost everywhere, at least in the daytime. The conditions in the free troposphere (cooler temperature, fewer pre-existing aerosols) will favour nucleation. (2) Nucleation maintains a reservoir of thermodynamically stable clusters (TSCs) which are too small to be detected. (3) Under certain conditions TSCs grow to detectable sizes and further to cloud condensation nuclei.

Two theoretically predictable pathways of atmospheric nucleation are ion induced²⁵ and ternary H_2SO_4 – NH_3 – H_2O (refs 4 and 24) mechanisms. The newly formed particles, whose sizes are greater than a critical cluster (about 1 nm) but are smaller than 3 nm, are called thermodynamically stable clusters. There are two possibilities for the growth of TSC particles to detectable size (> 3 nm in diameter). First, the concentration of pre-existing aerosols is low, owing perhaps to precipitation, self-coagulation of TSCs becomes significant and the growth to 3 nm size only takes an hour (see Fig. 2b). Second, if there is a high source of available condensable vapours (such as organics, inorganic acids and ammonia) growth through condensation to detectable sizes and even to Aitken mode size occurs over a timescale of about 1–2 hours (see Fig. 3).

There are distinct reasons why the existence of TSCs in the

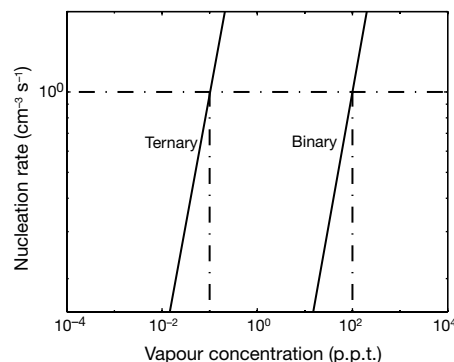


Figure 1 Nucleation rate as a function of sulphuric acid concentration for binary and ternary nucleation. The ambient sulphuric acid concentration (c_{amb}) needs to be three orders of magnitude higher in binary nucleation than in ternary nucleation in order to have the same nucleation rate (for example, $1 \text{ cm}^{-3} \text{ s}^{-1}$). The driving force in the condensation growth is proportional to $c_{\text{amb}} - c_s$, where c_s is the saturated vapour concentration at the droplet. For sulphuric acid, c_s is negligible compared to c_{amb} . Owing to the smaller vapour concentration needed for nucleation in the ternary nucleation scheme, the condensational growth of particles will be about 1,000 times slower than in the binary case.